Journal of Computational Physics **172,** 19–39 (2001)
doi:10.1006/jcph.2001.6751, available online at http://www.idealibrary.com on IDEAL®

Modeling Quantum Structures with the Boundary Element Method

F. Gelbard and K. J. Malloy

Center for High Technology Materials, University of New Mexico, Albuquerque, New Mexico 87131
E-mail: fgelbard@unm.edu

Received February 16, 2000; revised September 26, 2000

A detailed analysis of the boundary element formulation of the electronic states of quantum structures is presented. Techniques for minimizing computation time by reducing the number of boundary integrals, utilizing the repetitive nature of embedded multiple quantum structures, and eliminating boundary elements for modeling the effects of quantum wells that contain quantum structures are discussed. Boundary element solutions for isolated and coupled quantum wires and pyramidal quantum dots are presented. The results for the coupling of such quantum structures clearly show the splitting of ground and excited states into "bonding" and "antibonding" states for both wires and dots. The numerical algorithm is shown to accurately capture these symmetry properties of a system of quantum structures if the boundary element and quadrature points are properly organized. For an asymmetric system of coupled dots, depending on the energy level, the center of charge is shown to be either above or below that for a pair of uncoupled dots with the same dot separation and orientation. Results are also presented showing the increase in energy levels resulting from the additional confinement arising from placing quantum dots into a quantum well.

Key Words: quantum structures; quantum wires; quantum dots; boundary elements.

1. INTRODUCTION

Quantum effects begin to dominate as the size of semiconductor structures approaches the electron de Broglie wavelength. These structures are classified according to the dimensionality of the confinement, with quantum wires or quantum dots being confined in two or three dimensions, respectively.

Many of the previous numerical modeling approaches for these quantum structures used spatial discretization methods, such as the finite element or finite difference method [1, 2]. These methods are quite general but require considerable computational resources to model three-dimensionally confined structures. As an alternative, the boundary element method

0021-9991/01 $35.00

(BEM) is more efficient for systems that are governed by linear partial differential equations, such as Laplace's equation [3, 4], or Helmholtz's equation [5–8]. However, only in the past few years has the BEM been applied to quantum structures [9–13]. For perfectly matched crystalline materials without strain or scattering impurities, the single band model within the effective mass approximation for quantum structures reduces to Schrodinger's equation. Under these ideal conditions, Schrodinger's equation is identical to either the Helmholtz or Modified Helmholtz equation, both of which are suitable for analysis with the BEM.

In this work, we present the boundary element form of Schrodinger's equation for the electronic states of quantum structures embedded in a barrier material. The same boundary element formulation can be used for both quantum wires and quantum dots [11]. Particular attention is paid to reducing the computation time for evaluating boundary integrals by taking advantage of the element shape and the repetition of identical structures. As an example, we show that a pair of either two- or three-dimensionally confined quantum structures exhibits eigenstates analogous to molecular "bonding" and "antibonding" states. For these states, the electron probability density function is either symmetric and does not pass through zero, or is antisymmetric and passes through zero, respectively. These states can be readily obtained with the BEM if care is taken to construct a representation that retains the symmetry properties of the system.

The newly developed system of quantum structures placed within other quantum structures, such as dots placed in a one-dimensional quantum well, can also be efficiently modeled using the BEM. Because the barrier is now a flat layer, an exact Green's function can be developed that automatically incorporates the boundary conditions. By using this Green's function, we show that no boundary elements are required for the flat boundaries defining the quantum well, thus saving considerable computation time.

2. BOUNDARY ELEMENT FORMULATION FOR QUANTUM STRUCTURES

Consider a system of quantum structures embedded in a barrier material. A form of Schrodinger's equation in each material governs the envelope function, $\Psi(\vec{r})$, for a single band model within the effective mass approximation. Let the effective masses in the structure and barrier material be given by m_s^* and m_b^*, respectively. Then the governing equation in each region is

$$\nabla \cdot \left(\frac{1}{m_s^*} \nabla \Psi(\vec{r}) \right) + \frac{2E}{\hbar^2} \Psi(\vec{r}) = 0 \quad (\vec{r} \text{ within the structure}) \tag{1}$$

and

$$\nabla \cdot \left(\frac{1}{m_b^*} \nabla \Psi(\vec{r}) \right) + \frac{2}{\hbar^2} [E - U] \Psi(\vec{r}) = 0 \quad (\vec{r} \text{ within the barrier}), \tag{2}$$

where $|\Psi(\vec{r})|^2$ is the probability density of finding an electron at $\vec{r}$. The energy band offset in the barrier is given by the positive constant U, the eigenenergy of the system is given by $E > 0$, and $\hbar$ is Planck's constant divided by 2π. Because the electron exists in the region of interest, the envelope function is normalized such that

$$\int_V |\Psi(\vec{r})|^2 \, dV = 1, \tag{3}$$

where V is the spatial region of interest that includes all structures and the barrier.

At the interface between a quantum structure and the barrier, two conditions must be satisfied. These conditions are

$$\Psi \quad \text{continuous} \tag{4}$$

and

$$-\frac{1}{m_s^*}\nabla\Psi\cdot\vec{n} = \frac{1}{m_b^*}\nabla\Psi\cdot\vec{n}, \tag{5}$$

where $\vec{n}$ is the outer normal in the respective region. The boundary integral form [3, 4] of Eqs. (2) and (3) for constant values of m_s^* and m_b^* can be obtained using the standard procedure of multiplying Eqs. (2) and (3) by G_s and G_b, respectively, (the Green's functions in structures and the barrier, respectively), integrating over the respective regions, and using the following properties of the Greens' functions

$$\nabla'\cdot\nabla' G_s(\vec{r},\vec{r}') + k_s^2 G_s(\vec{r},\vec{r}') = -\delta(\vec{r},\vec{r}') \tag{6}$$

and

$$\nabla'\cdot\nabla' G_b(\vec{r},\vec{r}') - k_b^2 G_b(\vec{r},\vec{r}') = -\delta(\vec{r}-\vec{r}'), \tag{7}$$

where $\delta(\vec{r}-\vec{r}')$ is the Dirac Delta function and ∇' is the gradient operator with respect to the primed coordinate $\vec{r}'$. Because we are primarily interested in bound states for which $E < U$, we define the two constants in Eqs. (6) and (7) as the positive quantities

$$k_s^2 \equiv \frac{2m_s^* E}{\hbar^2} \tag{8}$$

and

$$k_b^2 \equiv \frac{2m_b^*(U-E)}{\hbar^2}. \tag{9}$$

With these definitions, the resulting boundary integral equations are

$$\eta(\vec{r})\Psi(\vec{r}) = \int_{\Gamma'} [G_s(|\vec{r}-\vec{r}'|)\nabla'\Psi(\vec{r}') - \Psi(\vec{r}')\nabla' G_s(|\vec{r}-\vec{r}'|)]\cdot\vec{n}'\,dS'$$

($\vec{r}$ lies within or on structures) (10)

and

$$\eta(\vec{r})\Psi(\vec{r}) = \int_{\Gamma'} [G_b(|\vec{r}-\vec{r}'|)\nabla'\Psi(\vec{r}') - \Psi(\vec{r}')\nabla' G_b(|\vec{r}-\vec{r}'|)]\cdot\vec{n}'\,dS'$$

($\vec{r}$ lies within or on the barrier), (11)

where $\eta(\vec{r})$ is 1, except when $\vec{r}$ is located on an interface and then it is equal to 1/2. The boundary integral in Eq. (10) is evaluated only over the interfaces of the structures in which $\vec{r}$ is located, and does not include other quantum structures. The boundary integral in Eq. (11), however, is evaluated over all structure interfaces because all quantum structures are exterior to the barrier. The outer normal and bounding surface of a region are given by $\vec{n}'$ and Γ', respectively. Integrations in Eqs. (10) and (11) are over the primed coordinates.

TABLE I
Green's Functions [14]

	$\nabla' \cdot \nabla' G_s + k_s^2 G_s = -\delta$	$\nabla' \cdot \nabla' G_b - k_b^2 G_b = -\delta$
Two-dimensional space	$\frac{i}{4} H_o^{(1)}[k_s \lvert \vec{r} - \vec{r}' \rvert]$	$\frac{1}{2\pi} K_o[k_b \lvert \vec{r} - \vec{r}' \rvert]$
Three-dimensional space	$\frac{\exp(ik_s \lvert \vec{r} - \vec{r}' \rvert)}{4\pi \lvert \vec{r} - \vec{r}' \rvert}$	$\frac{\exp(-k_b \lvert \vec{r} - \vec{r}' \rvert)}{4\pi \lvert \vec{r} - \vec{r}' \rvert}$

Note. K_o is the modified Bessel function, and $H_o^{(1)}$ is the Hankel.

For constant values of m_s^* and m_b^*, Eqs. (1) and (2), are also called the Helmholtz and modified Helmholtz equations, respectively. The free space Green's functions for these equations as given by Eqs. (6) and (7) are well known for two- and three-dimensionally confined systems [14], and are given in Table I. It is not required that the Green's functions satisfy interface or boundary conditions, and thus the analysis is simplified by using these free space Green's functions. (However, as will be shown later, considerable computational effort can be avoided by developing a Green's function that satisfies certain boundary conditions.) The boundary integral formulation for Helmholtz's equation has been extensively used for other applications [5–8].

Equations (10) and (11) may be approximated by discretizing all interfaces. In this work, interfaces for two- or three-dimensionally confined structures are discretized by constant elements, consisting of straight-line segments or triangular planes, respectively. The nodal points of these elements are located at the geometric center of the element. Because the quantum structures of interest are generally faceted surfaces, these simple element shapes can perfectly match the structure shape and thus do not introduce any geometry matching errors. Furthermore, for these element shapes, the gradient of the free space Green's function is orthogonal to the outer normal. Therefore, $\nabla' G(|\vec{r} - \vec{r}'|) \cdot \vec{n}'$ will always be zero for elements on the same facet with this type of Green's function. Thus, the second terms in the integrands in Eqs. (10) and (11) are zero under these conditions. These terms are also zero for the special case of a structure embedded in an infinite barrier (i.e, $U/E \to \infty$). For an infinite barrier, $\Psi = 0$ on the interface, and the envelope function in each structure is independent of Ψ in any other structure. (Infinite barriers are not achieved in practice, but are extremely useful for obtaining exact solutions for assessing the accuracy of numerical algorithms.)

The unknowns to be determined are the envelope function and the normal component of its gradient for each element on the interfaces. Let these be represented by Ψ_i and $\delta\Psi_i/\delta n'$, respectively, for element i. In this work, the quantum structures have the same shape, size, and orientation. Therefore, it is convenient to discretize just one such structure with N_e elements, and then replicate and translate this assembly to different positions for each additional structure. For N_s structures, the product $N_e N_s$ gives the total number of elements in the system. For systems with finite barriers, there are two unknowns in each element, and thus $2N_e N_s$ unknowns for the entire system. (Because the envelope function is identical in each structure for an infinite barrier, only one such structure needs to be simulated with N_e unknowns for $\partial\Psi_i/\partial n'$, $i = 1, \ldots, N_e$.)

In general, let X represent this vector of unknowns such that

$$X = \left[\Psi_1, \partial\Psi_1/\partial n', \Psi_2, \partial\Psi_2/\partial n', \ldots, \Psi_{2N_eN_s}, \partial\Psi_{2N_eN_s}/\partial n'\right]^T. \tag{12}$$

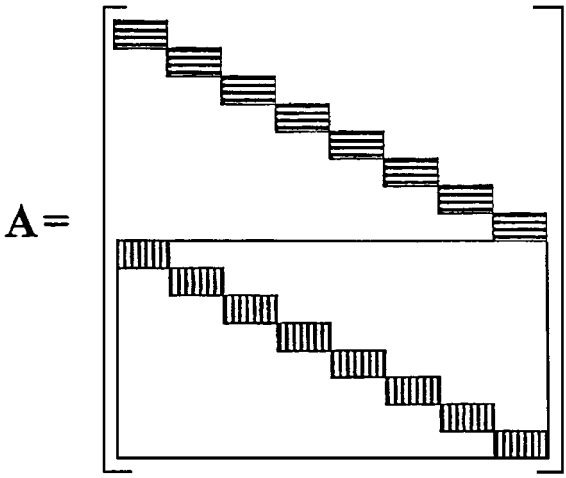

FIG. 1. BEM matrix form for eight quantum structures. The top and bottom halves of the matrix are from boundary element equations in the quantum structures and barrier, respectively. The matrix elements inside each structure have N_e rows and $2N_e$ columns and are represented by identical rectangular blocks that are filled with horizontal lines. The N_e by $2N_e$ rectangular blocks filled with vertical lines are also identical but different from those with horizontal lines. Matrix elements that are not enclosed by any rectangle are zero.

Then the system of equations to be solved is

$$AX = 0, \tag{13}$$

where A is a matrix of the form given in Fig. 1. (The matrix structure and solution methods for other multizone problems are discussed in [4].) The top and bottom halves of the matrix are from the boundary element equations for the quantum structures and barrier, respectively. The matrix elements for the boundary element equations inside each structure have N_e rows and $2N_e$ columns. These elements are represented in Fig. 1 by rectangular blocks that are filled with horizontal lines. Because these blocks of matrix elements are identical, only one such block of elements needs to be determined. (This would be true even if the structures had different orientations.) These matrix elements are given by

$$a_{i,2j-1} = -\frac{\delta_{i,j}}{2} - \int_{\Gamma'_j} \nabla' G_s(|\vec{r}_i - \vec{r}'|) \cdot \vec{n}' \, dS' \quad (i = 1, \ldots, N_e \quad \text{and} \quad j = 1, \ldots, N_e) \tag{14}$$

and

$$a_{i,2j} = \int_{\Gamma'_j} G_s(|\vec{r}_i - \vec{r}'|) \, dS' \quad (i = 1, \ldots, N_e \quad \text{and} \quad j = 1, \ldots, N_e), \tag{15}$$

where Γ'_j is the length of element j for two-dimensionally confined structures, or the area of element j for three-dimensionally confined structures. The nodal coordinates of element i are given by $\vec{r}_i$, the geometric center of the element, and $\delta_{i,j}$ is the delta function and is equal to 0 for $i \neq j$ and equal to 1 for $i = j$.

For the lower half of A, the matrix elements are given by

$$a_{i,2j-1} = -\frac{\delta_{i-N_eN_s,j}}{2} - \int_{\Gamma'_j} \nabla' G_b\left(\left|\vec{r}_{i-N_eN_s} - \vec{r}'\right|\right) \cdot \vec{n}'\, dS'$$

$$(i = N_eN_s + 1, \ldots, 2N_eN_s \quad \text{and} \quad j = 1, \ldots, N_eN_s) \quad (16)$$

and

$$a_{i,2j} = \int_{\Gamma'_j} G_b\left(\left|\vec{r}_{i-N_eN_s} - \vec{r}'\right|\right) dS' \quad (i = N_eN_s + 1, \ldots, 2N_eN_s \quad \text{and} \quad j = 1, \ldots, N_eN_s). \quad (17)$$

The lower half of A is fully dense. However, considerable work can be avoided by nothing that the N_e by $2N_e$ blocks of matrix elements corresponding to boundary elements on the same structure are identical. (This would be true even if the structures had different orientations.) These blocks are represented in Fig. 1 by rectangles filled with vertical lines. Thus,

$$a_{i+kN_e,j+2kN_e} = a_{i,j} \quad (i = N_eN_s + 1, \ldots, (N_s + 1)N_e) \quad (j = 1, \ldots, 2N_e) \quad (k = 1, \ldots, N_s - 1). \quad (18)$$

In this work, line integrals for two-dimensionally confined structures are determined by using an adaptive Gauss–Legendre quadrature algorithm. Surface integrals for three-dimensionally confined structures are determined using a 13-point Gauss–Legendre quadrature algorithm [4].

Of particular concern are coincident integrations in which the integration is over a boundary element that includes the nodal point $\vec{r}_i$ of that element. In this case, the integrand is singular at the nodal point. As noted previously, the outer normal to a surface is orthogonal to the gradient of the free space Green's function when the nodal point is on the same plane as the surface. Thus, the integrals in Eqs. (14) and (16) are zero when coincident. Furthermore, to reduce computation time, we also avoid evaluating noncoincident integrals in these equations whenever the nodal points and boundary elements are on the same line or the same plane, for two- and three-dimensionally confined structures, respectively.

For two-dimensionally confined structures, the coincident matrix elements $a_{i,2i}$ are determined by integrating term by term an analytic expansion of the integrand around the singularity. Coincident matrix elements in three-dimensionally confined structures are evaluated by transforming to polar coordinates with the origin at the singularity. Then each coincident triangle is divided by three lines that extend from the origin to each of the points of the triangle. The radial integration is performed analytically for each part of the divided triangle. The remaining integral in the angular direction is then evaluated numerically using an adaptive Gauss–Legendre quadrature algorithm. Analytical integration avoids the numerical problem of integrating over the region in which the Green's function is singular. The transformation to polar coordinates may also be used for elements that are on the same facet as the nodal point $\vec{r}_i$, but this was found to be computationally slower than the 13-point algorithm.

Not only the number of nodal and quadrature points but also the location of these points must be specified. For most applications, as long as the solution converges, and the nodal

and quadrature points uniformly cover the region of interest, the exact location of these points are not of great concern. However, for modeling systems of quantum structures, it is advantageous that system symmetries be contained in the numerical representation. Otherwise, we found that the envelope function did not accurately reflect the symmetry properties of the system, even though convergence was achieved. The problem is most prevalent for three-dimensionally confined structures such as a pyramidal dot in which 13 quadrature points are taken for noncoincident integrals. As will be shown in Section 4, the element shape, nodal points, and quadrature points should have the same rotational and reflection symmetries of the structure and the system of structures.

Once the matrix elements are evaluated using symmetrically located quadrature points, the system of equations may then be solved. However, this system as given by Eq. (13) is not a standard eigenvalue problem because the eigenenergy E is nonlinearly embedded in the matrix elements. Thus, to determine the eigenenergy we seek the values of E that make A singular so that Eq. (13) has a unique nontrivial solution. Because of machine inaccuracies, it is not practical to expect that A can be made exactly singular. Therefore, instead we use a simple spike finding algorithm to maximize the condition number of A by iterating on E. Once an eigenenergy is determined, the null space can be determined using a singular value decomposition (SVD) of A. (In this work, the routine ZGECON [15] is used to compute the complex double precision condition number, and ZGESDD or CGESDD [15] are used to determine the double or single precision singular value decomposition, respectively.) We do not use SVD for determining the conditioning of A because it is generally slower than estimating the condition number. Degenerate states are readily available with only one SVD because these states have the same singular values. In practice, we found that for degenerate states the smallest singular values are identical to five or more significant figures. Furthermore, the null space is clearly distinguishable because the smallest singular values that represent the null space are usually at least one or two orders of magnitude smaller than any other singular value. The envelope function at any point within the system is then determined by substituting the null vector into Eq. (10) for points within a structure, or Eq. (11) for points within the barrier.

Each of the three computational steps described above has different work requirements. Determining the condition number and the boundary element values requires on the order of a minute to tens of minutes on a personal computer operating at 266 MHz. This step requires evaluating approximately $2N_e^2(1 + N_s^2)$ boundary integrals, and evaluating the condition number for each of these sets of boundary integrals. The second step requires performing a singular value decomposition, and can be readily performed using an available code package. For the third step, N_e or N_sN_e boundary integrals are evaluated to determine the envelope function in a structure or in the barrier, respectively. The work for the three steps is thus dependent on the number of elements per structure, the number of structures, and the level of detail needed for the envelope function. We typically use only 20 to 320 boundary elements for each structure, and 10^4 to 10^5 spatial points to get a detailed envelope function. For moderate problems with on the order of 50 elements and 10^4 spatial points, the entire problem can be completed and plotted on a PC in less than about 10 minutes.

3. TWO-DIMENSIONALLY CONFINED STRUCTURES

Figure 2 is a plot of the condition number of matrix A for 40 elements as a function of E, the eigenenergy for a square quantum wire that is 10 nm by 10 nm, embedded in

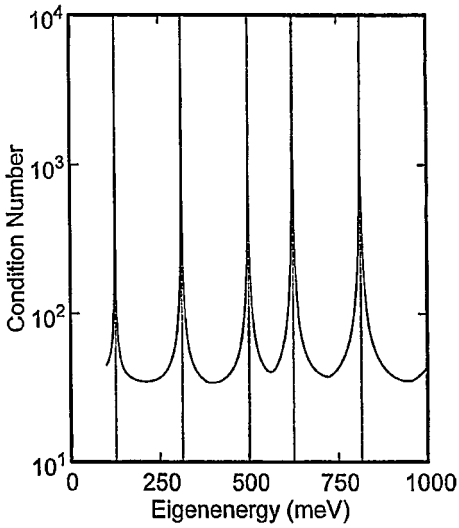

FIG. 2. Condition number spectrum for a 10-nm square wire with $m^* = 0.06m_e$ in an infinite barrier with 40 boundary elements. Exact values are plotted as broken vertical lines at 125.34, 313.36, 501.37, 626.72, and 814.73 meV.

an infinite barrier. For convenience, the effective masses in all calculations throughout this work in both the barrier and the structure are taken as $0.06m_e$, where m_e is the rest mass of an electron. The exact eigenenergies for this simple case are given in the figure caption and plotted as vertical broken lines in the figure. Notice that the spikes in condition number of the matrix coincide with the eigenenergies. As reported previously [11], the relative error in the computed eigenenergies decreases quadratically with the inverse of the number of elements. However, the computational work does not scale linerarly with the number of elements, and thus the relative error does not decrease quadratically with computation time. Consider the fully dense matrices that result for a single quantum structure. If a direct linear solver is used, the work increases as the cube of the number of boundary elements, and therefore the relative error decreases only as the $-2/3$ power of the computation time. Fortunately, BEM solutions require few elements to obtain accurate results. We found that for 40 elements the eigenenergies are accurate to more than three significant digits. Such accuracy can be obtained in about a minute of computation time on a personal computer operating at 266 MHz. We therefore did not explore other solvers for determining the condition number, or utilize the sparseness of the matrix given in Fig. 1 for multistructure systems. For the remaining figures, results in two confining dimensions will be shown with 40 elements for each structure.

The results for a realistic system that includes a finite barrier with $U = 300$ meV are shown in all the remaining figures. (A convenient summary of all the cases presented in the figures is given in Table II.) For the 10-nm square wire in a finite barrier, the two lowest eigenenergies computed using the search algorithm are 74.2 and 179 meV. The first excited state at $E = 179$ meV is doubly degenerate. This degeneracy is due to the symmetry of the system that is invariant to a 90-degree rotation. Each degenerate state can be constructed to consist of two probability lobes that are at diametrically opposite corners of the square. For later comparisons, we took a linear combination of the two null vectors to obtain another linearly independent set of degenerate states. This set has the probability lobes aligned

TABLE II
Summary of Cases Presented

System	State	Spacing	Figure
1 wire	excited	—	3
2 wires	σ-antibonding	2 nm horizontal	4a
2 wires	σ-bonding	2 nm horizontal	4b
2 wires	π-antibonding	2 nm horizontal	4c
2 wires	π-bonding	2 nm horizontal	4d
1 dot	ground	—	7
1 dot	excited	—	8
2 dots	σ-antibonding	2 nm horizontal	9a
2 dots	σ-bonding	2 nm horizontal	9b
2 dots	π-antibonding	2 nm horizontal	9c
2 dots	π-bonding	2 nm horizontal	9d
2 dots	ground antibonding	1 nm vertical	10a
2 dots	ground bonding	1 nm vertical	10b
2 dots	(ground bonding)–(ground antibonding)	1 nm vertical	10c

vertically or horizontally. A contour plot of the vertically aligned lobes is shown in Fig. 3. The other degenerate state consisting of horizontally aligned lobes can be obtained by a 90-degree rotation of Fig. 3.

For our work we are interested in the interaction between quantum structures. The results that we now present for quantum wires will be useful for understanding quantum dots. Consider two 10-nm square quantum wires that are placed 2 nm apart, and are centered at ($x = -6$ nm, $y = 0$, $z = 0$) and ($x = 6$ nm, $y = 0$, $z = 0$). The system of two wires breaks the four-fold rotational symmetry and the first excited state splits into four different states

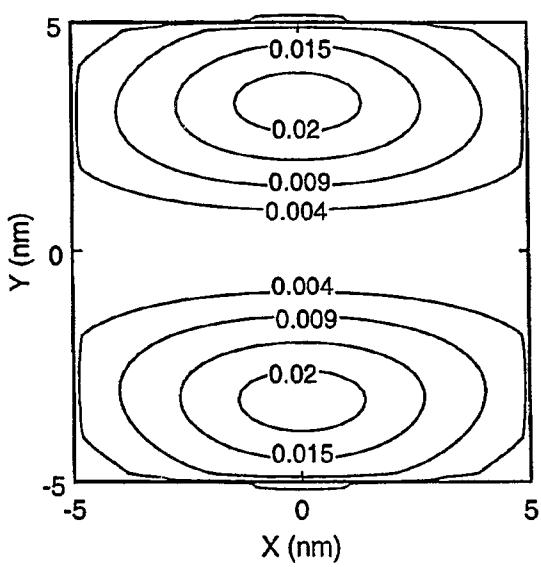

FIG. 3. Contour plot of normalized probability density for a degenerate excited state at E = 179 meV in a 10 nm-square wire embedded in a barrier with U = 300 meV. The contour levels shown are in nm^{-2}.

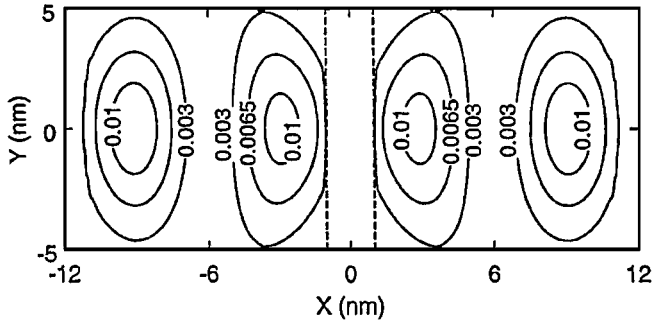

FIG. 4a. Contour plot of normalized probability density for two 10 nm square wires separated by 2 nm along the x-axis. Shown is the σ-antibonding state (E = 196 meV). The contours from the outer edge of the wires inwards are for 0.003, 0.0065, and 0.01 nm^{-2}. The vertical dotted lines correspond to the edges of the wires.

shown in Figs. 4a–4d. Each of these four states will be either antisymmetric or symmetric about the plane x = 0. By analogy to molecular systems, the envelope functions in the plane x = 0 must therefore respectively be either zero indicating an "antibonding" state, or be nonzero indicating a "bonding" state. The highest excited state at E = 196 meV is shown in Fig. 4a. We call this state the "σ-antibonding" state because the envelope function is identically zero at x = 0, and the probability density lobes are oriented along a line joining the center of the wires. We call the lowest excited energy state at E = 164 shown in Fig. 4b the "σ-bonding" state. In this state the envelope function is symmetric about x = 0. By comparing Figs. 4a and 4b, we note that the probability densities in each wire are shifted away from or toward those in the adjacent wire, for the antibonding or bonding states, respectively.

The two intermediate states at E = 184 meV and E = 174 meV, are shown in Figs. 4c and 4d, respectively. Because the probability density lobes are oriented perpendicular to the line joining the wires, and the envelope function is either antisymmetric or symmetric, we call these states "π-antibonding" and "π-bonding," respectively. Similar to the σ-states, for the π-states the high electron probability density lobes in adjacent wires are further for the higher energy state given in Fig. 4c than for that in Fig. 4d. Both the σ-antibounding and the π-antibounding states have a zero probability density in the plane x = 0.

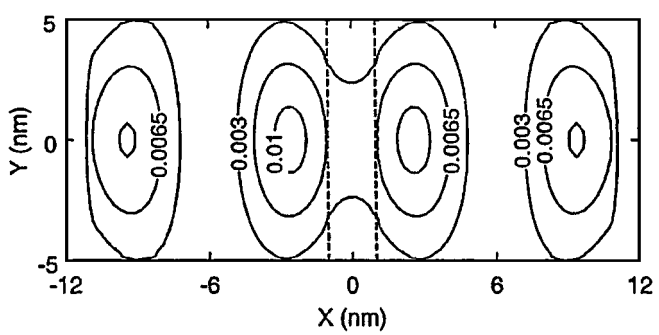

FIG. 4b. Contour plot of normalized probability density for two 10 nm-square wires separated by 2 nm along the x-axis. Shown is the σ-bonding state (E = 164 meV). Compared to Fig. 4a, note the higher probabilities in the regions where the wires are closest. The contours from the outer edge of the wires inwards are for 0.003, 0.0065, and 0.01 nm^{-2}. The vertical dotted lines correspond to the edges of the wires.

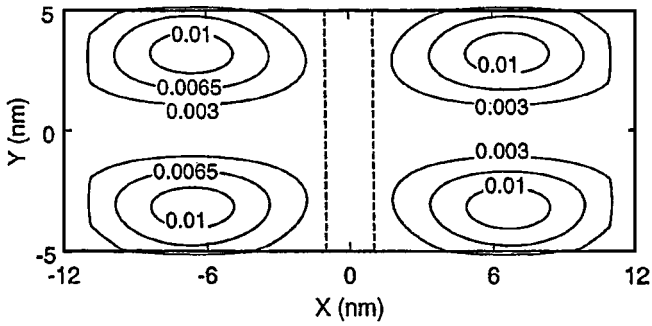

FIG. 4c. Contour plot of normalized probability density for two 10 nm-square wires separated by 2 nm along the x-axis. Shown is the π-antibonding state (E = 184 meV). The contours from the outer edge of the wires inwards are for 0.003, 0.0065, and 0.01 nm^{-2}. The vertical dotted lines correspond to the edges of the wires.

4. THREE-DIMENSIONALLY CONFINED STRUCTURES

The quantum dots of interest are assumed to be pyramidal in shape with a base length that is twice that of the height [1]. Using the BEM formulation discussed previously, we now present results for such dots in a 300 meV barrier with dot dimensions as given in Fig. 5, and with 320 elements for each dot. The differences in eigenenergy using 160 or 320 elements per dot were less than one percent.

As discussed previously, it is advantageous that the numerical representation retain the symmetry properties of the system. Thus, to start the discretization process, each triangular side of the pyramid is used as a triangular element, and the base is divided into four identical triangles formed by two diagonal lines that cross the base. At this point, each element consists of an isosceles triangle, and all the rotational symmetry properties of the structure are contained in the numerical representation with a total of eight elements. As shown in Fig. 6, to refine this representation each isosceles triangle can then be divided into four identical isosceles triangles by drawing a horizontal line that is half way between the base and the apex, and using that line as the base for an inverted isosceles triangle. This refinement process quadruples the number of elements into smaller identical elements, while still retaining the symmetry properties of the original triangle.

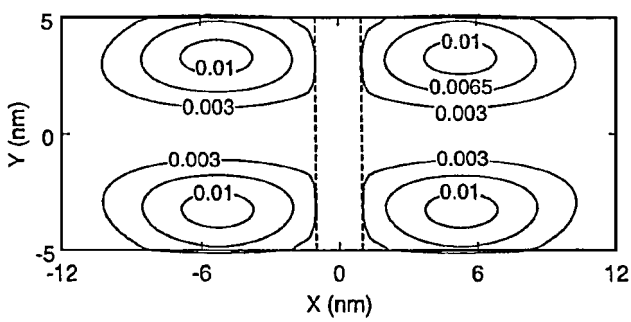

FIG. 4d. Contour plot of normalized probability density for two 10 nm-square wires separated by 2 nm along the x-axis. Shown is the π-bonding state (E = 174 meV). Compared to Fig. 4c, note the higher probabilities in the regions where the wires are closest. The contours from the outer edge of the wires inwards are for 0.003, 0.0065, and 0.01 nm^{-2}. The vertical dotted lines correspond to the edges of the wires.

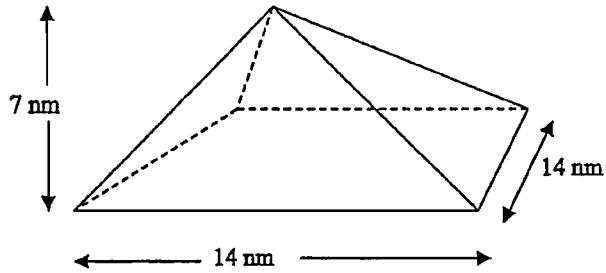

FIG. 5. Pyramidal quantum dot.

Any of the three triangular points may be taken as the origin of the natural coordinates for determining Gaussian quadrature points in these triangles. However, to ensure that the quadrature points are also symmetric, the origin of the natural coordinates is taken as the apex of the triangle. Because all elements are isosceles triangles, and the quadrature points and weighting factors are symmetric with respect to the natural coordinates, using the apex as the origin guarantees that all quadrature points will be symmetrically located within the element. This process of dividing one triangle into four identical triangles and using apex-originated quadrature points may be repeated indefinitely and still preserve all symmetries.

In addition, each triangle may be divided in half by a line from the apex to the midpoint of the base. This refinement will also retain all symmetry properties if the original apex is used as the origin for both halves. However, this step can only be performed once, and may only be the last refinement step. The reason why we introduce this step is to provide more flexibility for allowing the number of elements to increase by an integer power of 2, instead of only an integer power of 4.

For a pyramidal dot, elements on the sides of the pyramid have a larger area compared to those on the base. Thus, we delay refining elements on the base until there is a total of 16 elements on the sides of the pyramid. For the same number of elements, there is no difference in computation time when using the above-described symmetric discretization procedure. However, as will be discussed, there is a dramatic improvement in the accuracy of the probability densities at the planes of symmetry when using this procedure.

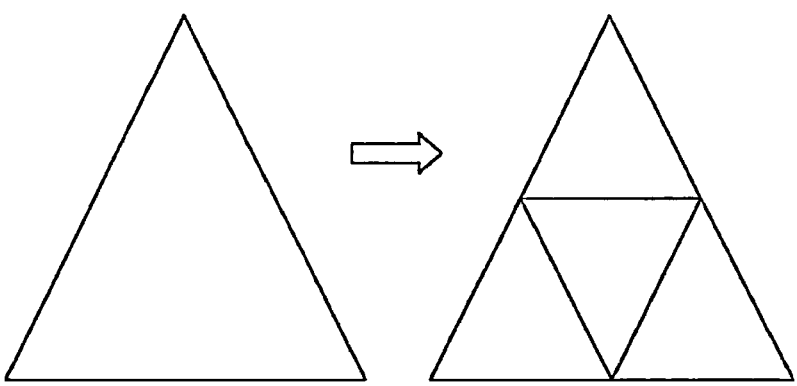

FIG. 6. Symmetrically refined triangular element.

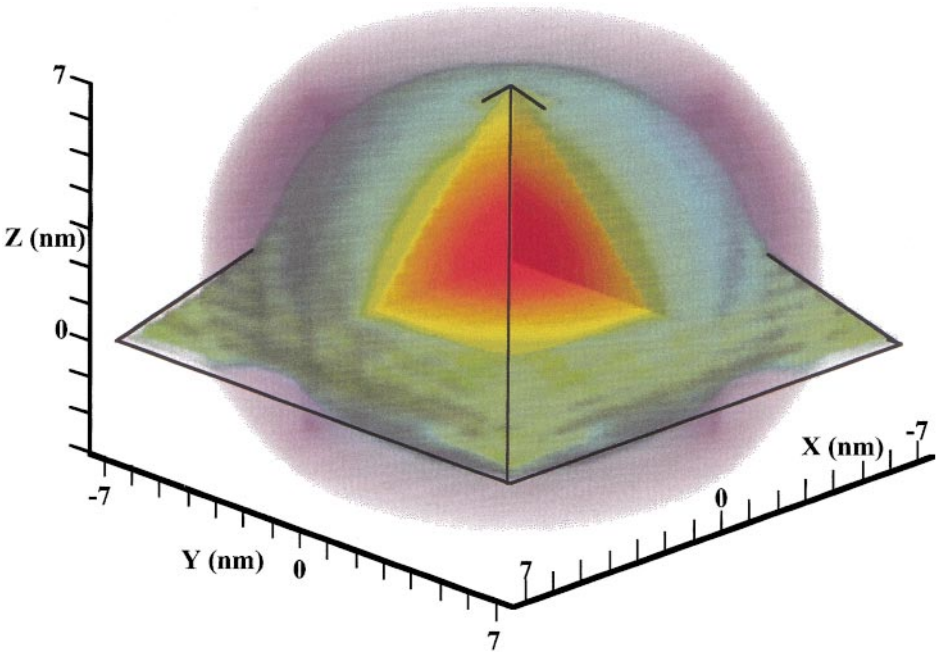

FIG. 7. Logarithm of normalized probability density for ground state at E = 184 meV in a pyramidal dot with a base length of 14 nm and height of 7 nm computed with 320 boundary elements. A wire frame of the dot is superimposed on the probability density. A portion of the density function has been removed to reveal interior values. The color ranges from red to translucent purple, which represents the range from 7.8×10^{-3} to 10^{-7} nm^{-3}.

By using the just described discretization procedure, we calculated that only three bound energy states exist for a dot of dimensions given in Fig. 5. The logarithm of the normalized probability density for the ground state at E = 184 meV is shown in Fig. 7, and is 90-degrees rotationally symmetric. The regions vary from red to translucent purple corresponding to $|\Psi|^2$ ranging from 7.8×10^{-3} to 10^{-7} nm^{-3}, respectively. We display $\log_{10}|\Psi^2|$ instead of $|\Psi|^2$ so as to reveal the small but not insignificant values extending beyond the dot boundaries that will show either bonding or antibonding features of multiple structures. A wire frame of the dot is superimposed on the probability density. In this figure, the center of the pyramid is at the origin and the triangular sides are aligned parallel to either the x- or y-axis. The pyramid base lies on the plane z = 0 and a corner has been removed from the probability density lobe to reveal the high probability density of the interior. Most of the probability is confined to the dot, but as shown in Fig. 7, a considerable amount extends about 2 nm below the base. The ridges on the surface are due to the discretization of the plotting software for which only 30 layers are used in the *z*-direction.

More interesting is the excited state which is doubly degenerate at E = 282 meV. One of the degenerate states is shown in Fig. 8. (The second degenerate state can be obtained by rotating the figure 90 degrees about the z-axis.) The lobes in Fig. 8 are symmetric in the plane x = 0. The left lobe in the figure has been partially removed to reveal interior values of the probability density. Notice that some of the probability density extends beyond the triangular sides of the dot.

Determining the exact dimensions of quantum structures is not an easy task. However, we can readily simulate changes in energy states for a wide range of dot sizes. As shown in

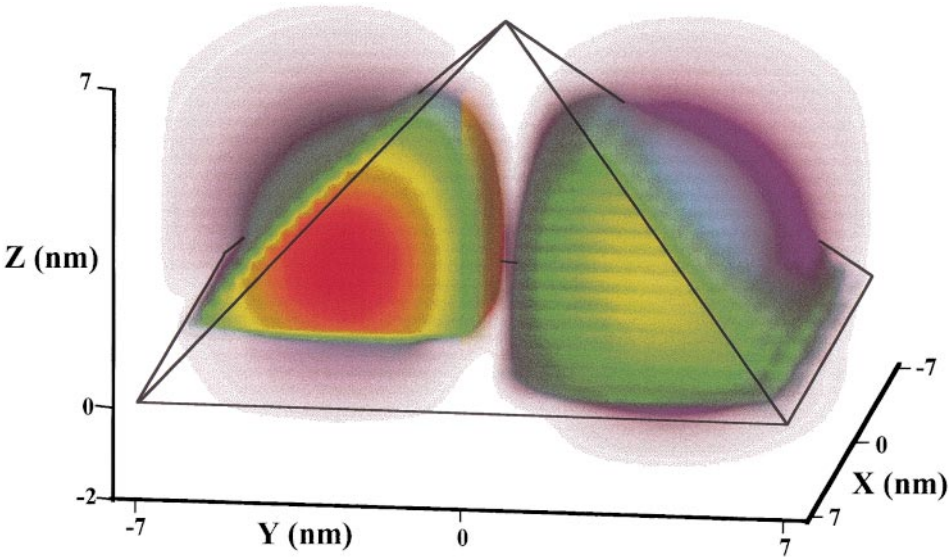

FIG. 8. Logarithm of normalized probability density for first excited state at E = 282 meV in a pyramidal dot. The left lobe has been partially removed to reveal interior values. The lobes are mirror images along the plane $y = 0$. The other degenerate state at this energy can be obtained by rotating this image 90 degrees about the z-axis. The color ranges from red to translucent purple, which represents the range from 6.9×10^{-3} to 10^{-7} nm^{-3}.

Fig. 9, the lowest two eigenenergies are plotted as a function of pyramidal height with the pyramidal base length maintained at twice that of the height. As the dot size decreases, the eigenergy increases with the excited state no longer bound to the dot for dot heights less than about 6.6 nm.

Exhibiting behavior similar to interacting quantum wires, quantum dots present a still richer set of phenomena. In Figs. 10a–10d two dots are placed 2 nm apart in the x-direction. In these figures the dots have the same orientation and shape as given in Fig. 5, but the origins of the dots are displaced in the x-direction by 8 nm and -8 nm, respectively. Just as with

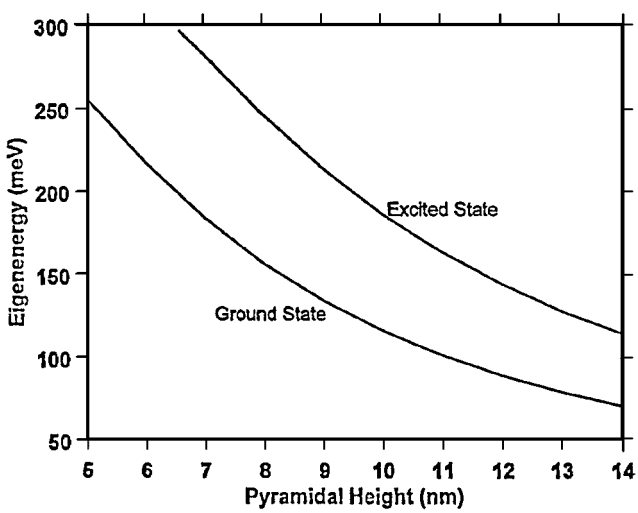

FIG. 9. Variation of eigenenergy with dot size for a pyramidal dot with a base length twice that of the height.

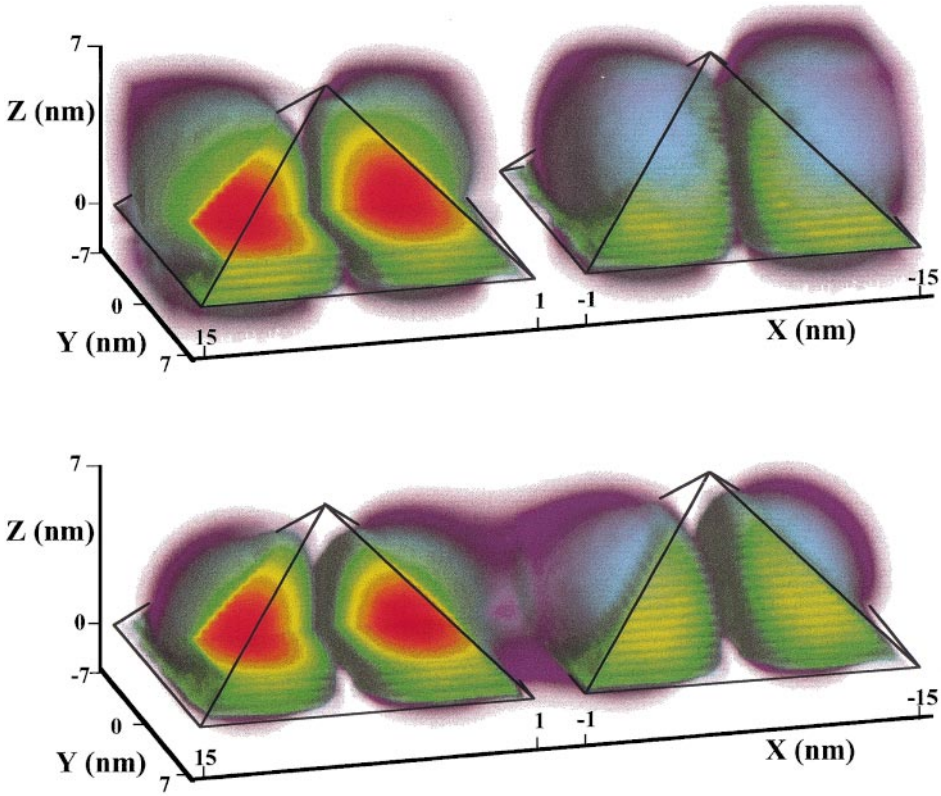

FIG. 10a. Logarithm of normalized probability density for two pyramidal dots separated by 2 nm in the x-direction. The σ-antibonding state at E = 289 meV is shown. The lobes are mirror images along the plane x = 0. The two lobes in the dot positioned at x > 0 have been partially removed to reveal interior values. Lobes that are furthest from the adjacent dot have a higher probability density than the lobes that are closest to the adjacent dot. The color ranges from red to translucent purple, which represents the range from 3.4×10^{-3} to 10^{-7} nm^{-3}.

FIG. 10b. Logarithm of normalized probability density for two pyramidal dots separated by 2 nm in the x-direction. The σ-bonding state at E = 277 meV is shown. The two lobes in the dot positioned at x > 0 have been partially removed to reveal interior values. Notice in comparing to Fig. (10a) that the lobes closest to the adjacent dot have a higher probability density than the more distant lobes. The color ranges from red to translucent purple, which represents the range from 3.4×10^{-3} to 10^{-7} nm^{-3}.

quantum wires, in these figures the probability densities are symmetric in the plane x = 0, and the doubly degenerate excited state splits into four nondegenerate states. In Figs. 10a and 10b, the corresponding σ-antibonding and σ-bonding states are shown, respectively. These are similar to Figs. 4a and 4b, in that the probability densities are zero or nonzero, respectively, in the plane x = 0, and the densities are lowest near adjacent structures for the highest energy. In Fig. 10b, bonding results in the probability density extending even further from the triangular side shown in Fig. 8, such that there is a tunneling of probability between the dots. In Fig. 10a, for the antibonding state there is a void in probability density between the dots. Also, similar to Figs. 4c and 4d, in Figs. 10c and 10d, respectively, we show the π-antibonding and π-bonding states. In Fig. 10d, bonding is shown by the tunneling of probability between the dots, and there is a corresponding void between the dots for the antibonding state shown in Fig. 10c. If the symmetric discretization procedure is not used,

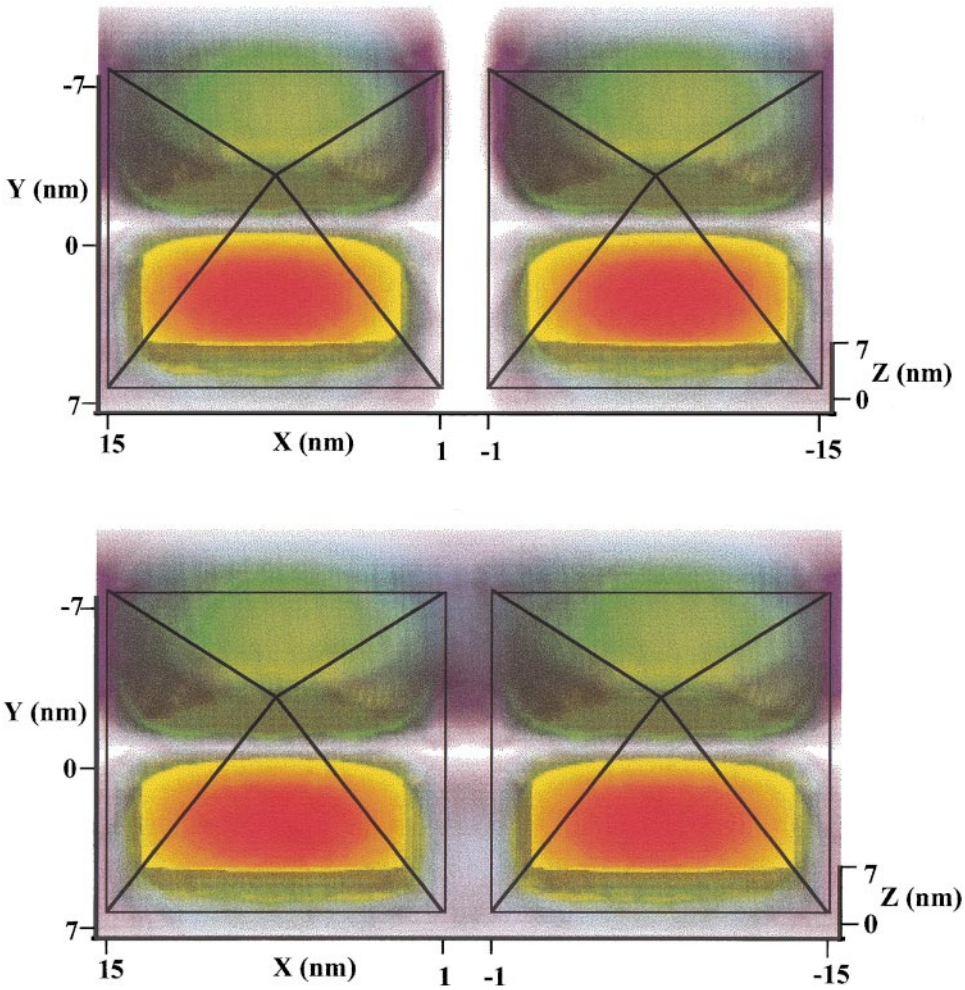

FIG. 10c. Logarithm of normalized probability density for two pyramidal dots separated by 2 nm in the x-direction. The π-antibonding state at $E = 284$ meV is shown. The two lobes positioned at $y > 0$ have been partially removed to reveal interior values. The color ranges from red to translucent purple, which represents the range from 3.5×10^{-3} to 10^{-7} nm^{-3}.

FIG. 10d. Logarithm of normalized probability density for two pyramidal dots separated by 2 nm in the x-direction. The π-bonding state at $E = 280$ meV is shown. The two lobes positioned at $y > 0$ have been partially removed to revel interior values. The color ranges from red to translucent purple, which represents the range from 3.5×10^{-3} to 10^{-7} nm^{-3}.

the probability density in the plane $x = 0$ is about 10^{-6} to 10^{-7} nm^{-3} compared to values of on the order of 10^{-3} nm^{-3} at the highest density values. A drop of several orders of magnitude of the probability density at $x = 0$ compared to the highest probability density in the problem, for both the bonding and antibonding states, is not indicative of the symmetry of the system. However, by using the symmetric discretization and quadrature procedure, the probability density at the symmetry plane for only the antibonding states drops to about 10^{-30} or 10^{-15} nm^{-3} if the SVD is computed in double or single precision, respectively. Similarly, the bonding state is symmetric to at least five significant figures. This dramatic

improvement provides a method for discerning the bonding or antibonding states in systems of quantum structures without requiring any additional computation time.

Pyramidal dots may also be stacked vertically along their axis of rotation [16, 17]. The two lowest energy states that result from the coupling of two vertically separated pyramidal dots are shown in Figs. 11a and 11b. For 1 nm separation the antibonding and bonding states have eigenenergies of 195 and 173 meV, respectively. For the bonding state shown in Fig. 11b, the probability density fills the gap between the dots, which does not occur as much for the antibonding state shown in Fig. 11a. For the antibonding state, the probability densities shift away from the adjacent dot. Because the effect on the ground state probability density for such a stacking is small, the shift in this density can be displayed by taking the difference in probability density for the lower energy state, minus that at the higher energy state. This difference is shown in Fig. 11c. The disparate shapes for the density difference is asymmetric, and clearly reveals that the lower energy state has a higher probability density in the upper part of the lower dot.

The asymmetry of vertically stacked pyramidal quantum dots also has the interesting effect of shifting the center of charge of the system. If the dots are uncoupled, the center of charge z_o, can be determined from

$$0 = \int_{-\infty}^{\infty}\int_{-\infty}^{\infty}\int_{-\infty}^{\infty}(z - z_o)[|\Psi_{\text{isolated}}(x, y, z)|^2 + |\Psi_{\text{isolated}}(x, y, z - \Delta)|^2]\,dx\,dy\,dz, \qquad (19)$$

where Δ is the vertical displacement of the dots, and $|\Psi_{\text{isolated}}(x, y, z)|^2$ is the probability

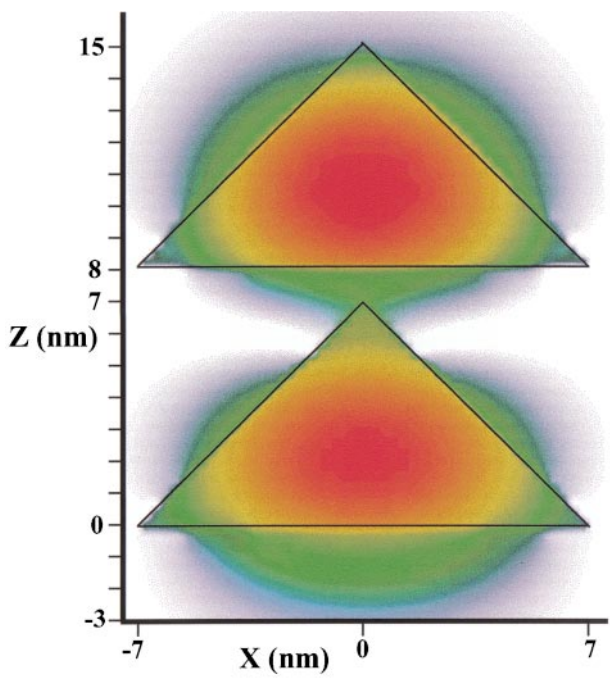

FIG. 11a. Logarithm of normalized probability density for two pyramidal dots vertically separated by 1 nm. The antibonding state at E = 195 meV is shown. The region $y > 0$ has been removed. The color ranges from red to translucent purple, which represents the range from 3.8×10^{-3} to 10^{-7} nm^{-3}. The region $y > 0$ has been removed.

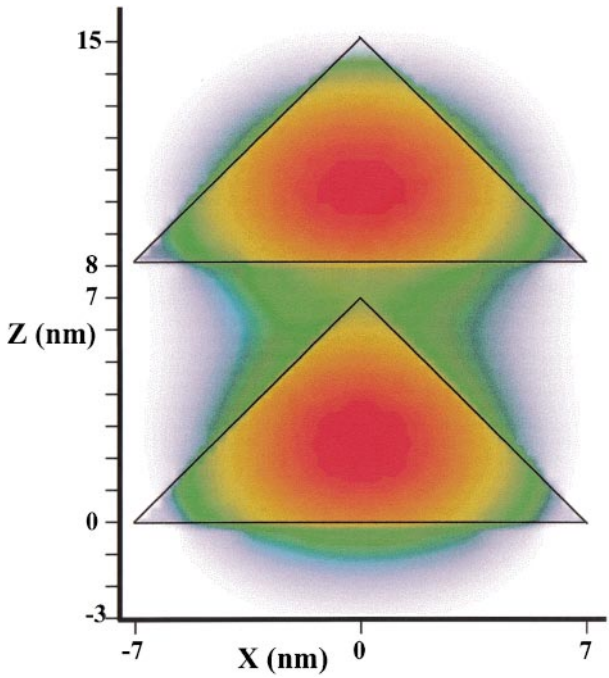

FIG. 11b. Logarithm of normalized probability density for two pyramidal dots vertically separated by 1 nm. The bonding state at E = 173 meV is shown. The region $y > 0$ has been removed. The color ranges from red to translucent purple, which represents the range from 4.2×10^{-3} to 10^{-7} nm^{-3}.

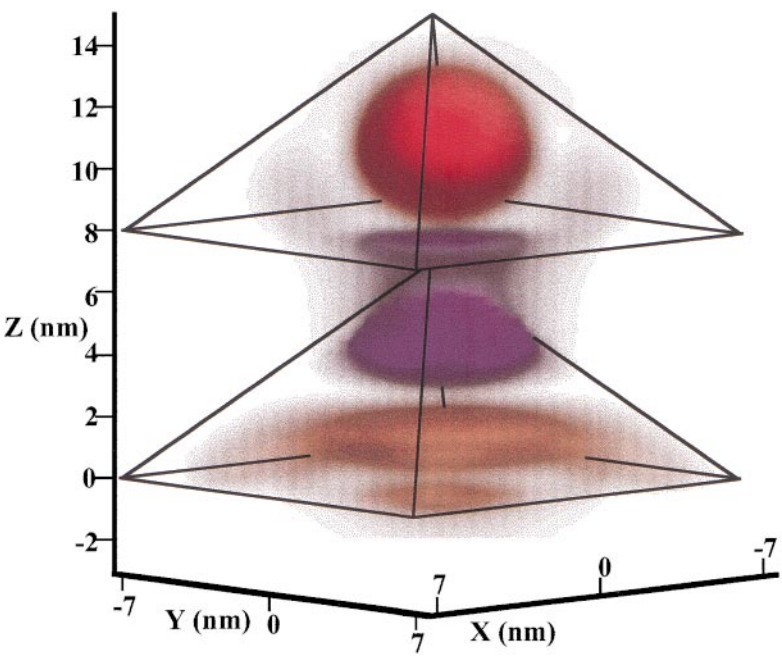

FIG. 11c. Difference in normalized probability density at E = 173 meV minus that at E = 195 meV for vertically stacked pyramidal quantum dots separated by 1 nm. The red spherical and reddish brown regions correspond to negative values, and the blue region corresponds to positive values.

density for an isolated dot as given in Fig. 7. If coupled dots are viewed as molecular systems, then the displacement of the center of charge for coupled dots can be given by

$$D = \int_{-\infty}^{\infty}\int_{-\infty}^{\infty}\int_{-\infty}^{\infty}(z - z_o)\Psi_{coupled}(x, y, z)|^2\, dx\, dy\, dz, \tag{20}$$

where $|\Psi_{coupled}(x, y, z)|^2$ is the probability density for coupled dots. Because the probability density decays rapidly away from the dots, the infinite ranges of integrations indicated in Eqs. (19) and (20) are taken only over a computational domain. For an isolated dot, this domain is a rectangular solid region from 3 nm below the pyramid to the top of the pyramid, and from -7.5 nm to 7.5 nm in the *x*- and *y*-directions. The domain for vertically stacked dots is from 3 nm below the bottom pyramid to the top of the top pyramid, and with the same range in the *x*- and *y*-directions as for an isolated dot. In the limit of large spacing between the dots, there is no coupling and the center of charge is halfway between the center of charges for the individual dots. However, for the coupled system with 1 nm vertical spacing from Eq. (20) the displacements of the center of charge relative to that for two uncoupled dots, are $D = 0.031$ nm at $E = 173$ meV and $D = -0.0064$ nm at $E = 195$ meV. For the lower energy state, the distance-weighted probability density in the lower dot shifts to higher values more than the amount this quantity is lowered in the upper dot. Hence, the lower energy state has a positive displacement of the center of charge. However, for the higher energy state, the distance weighted probability density in the lower dot decreases more than that in the upper dot, resulting in a negative displacement of the center of charge.

5. QUANTUM WELL CONFINEMENT OF THREE-DIMENSIONALLY CONFINED QUANTUM STRUCTURES

Quantum dots may also be grown inside a quantum well [18, 19]. This system allows one to further control confinement, and thereby vary the bound states for pyramidal dots. In the discussions given above, we presented results for a finite energy barrier of infinite extent. Now we consider a finite layer of barrier material of thickness L bounded by the planes $z = 0$ and $z = L$. Inside this layer, we center a pyramidal dot with the base of the pyramid parallel to the plane $z = 0$, such that the distance from the pyramid base to the plane $z = 0$ is the same as the distance from the pyramid apex to the plane $z = L$. To determine the maximum effect of the quantum well, we present results for a well with an infinite energy barrier. Thus, the envelope function is zero at the bounding planes $z = 0$ and $z = L$.

If the free space Green's function is used in Eq. (11), then in addition to integrating over the surfaces of the dots, the integration must also include the bounding planes $z = 0$ and $z = L$. This would require numerous elements for the bounding planes and significantly add to the number of unknowns to be determined. However, an elegant way to avoid discretizing the bounding planes is to develop a special Green's function [20] that satisfies Eq. (11) and the homogeneous condition $G_b = 0$ on these planes. By using the method of images, this Green's function is given by

$$G_b(\vec{r}, \vec{r}') = G_{-00} - G_{+00} + \sum_{n=2}^{\infty} G_{-+n} + G_{--n} - G_{+-n} - G_{++n}, \tag{21}$$

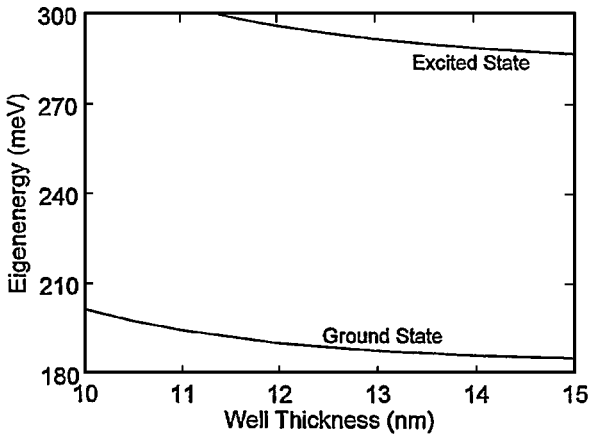

FIG. 12. Bounded eigenenergies of a pyramidal quantum dot as a function of the well thickness L. In the limit of $L \to \infty$, the ground and excited state energies approach 184 meV and 282 meV, respectively. At $L = 11.5$ nm the excited state exceeds the barrier energy of 300 meV.

where

$$G_{pqn} = \frac{\exp(-k_b\sqrt{(x' - x)^2 + (y' - y)^2 + (z' + pz + 2qnL)^2})}{4\pi\sqrt{(x' - x)^2 + (y' - y)^2 + (z' + pz + 2qnL)^2}}, \tag{22}$$

and the Cartesian components of $\vec{r}$ and $\vec{r}'$ are given by (x, y, z) and (x′, y′, z′), respectively. Because $G_b = 0$ and $\Psi = 0$ on the bounding planes, the integrand in Eq. (11) is zero on these planes when integrating over the primed coordinates. Therefore, there is no need to introduce any unknowns for these planes. Thus, the size and form of the matrix A given in Eq. (13) is the same regardless of whether or not a quantum well is included. However, $\nabla' G_b(\vec{r}, \vec{r}') \cdot \vec{n}'$ is no longer zero when $\vec{r}'$ and $\vec{r}$ are on the same facet, and thus the second term of the integrand in Eq. (11) must now be computed when integrating over the surfaces of dots. This is a small computational expense to pay for the tremendous savings obtained by eliminating the bounding plane elements.

By using the special Green's function in Eq. (21), we show in Fig. 12 the effect on the eigenenergy as the well thickness L, varies from 10 nm to 15 nm for a pyramidal dot that has the dimensions given in Fig. 5, and is centered within the well. In the limit of L much greater than the dot dimensions, the eigenenergies approach the values given previously. However, as the well thickness decreases, the additional confinement increases the bound state eigenenergies. As shown in Fig. 12, at a well thickness of about 11.5 nm, the excited state energy exceeds the barrier energy of 300 meV. Thus, the excited state is no longer bound to the dot, and only the ground state exists in the dot.

6. CONCLUSIONS

In this work, we analyzed application of the boundary element method (BEM) to quantum structures. A multizone implementation of the BEM was analyzed to minimize the computation of matrix elements. Application of the technique to two- and three-dimensionally confined quantum structures was presented. For both cases, when two structures interact,

the eigenstates of isolated structures split into bonding and antibonding states, with the bonding state having the lower energy. For pyramidal dots, the coupling was shown to be dependent on the relative orientation of the dots. Furthermore, we showed that by using a special Green's function, the confining effects of a quantum well on quantum dots can be incorporated into a boundary element algorithm without requiring any elements on the boundaries of the quantum well. Thus, the matrix size and hence the time for computation of the condition number, null space, and envelope function are not dependent on the inclusion of a quantum well. Because modeling such systems with the BEM can be performed in minutes on a personal computer to an accuracy of a few percent, the method is highly attractive compared to the more traditional domain discretization approaches.

ACKNOWLEDGMENTS

The first author thanks Professor Marc Ingber of the University of New Mexico, and Dr. Samuel Subia of Sandia National Laboratories for very helpful discussions on the boundary element method.

REFERENCES

1. M. Grundmann, O. Stier, and D. Bimberg, *Phys. Rev. B* **52**, 11969 (1995).
2. O. Stier, M. Grundmann, and D. Bimberg, *Phys. Rev. B* **59**, 5688 (1999).
3. C. A. Brebbia and J. Dominguez, *Boundary Elements: An Introductory Course*, 2nd ed. (McGraw-Hill, New York, 1992).
4. J. H. Kane, *Boundary Element Analysis in Engineering Continuum Mechanics* (Prentice Hall, Englewood Cliffs, NJ, 1993).
5. R. E. Kleinman and G. F. Roach, *SIAM Rev.* **16**, 214 (1974).
6. R. P. Shaw, Boundary integral equation methods applied to wave problems, in *Developments in Boundary Element Methods—1*, edited by P. K. Banerjee and R. Butterfield (Applied Science, London, 1979).
7. A. F. Seybert, B. Soenarko, F. J. Rizzo, and D. J. Shippy, *J. Acoust. Soc. Am.* **77**, 362 (1985).
8. M. S. Ingber and C. E. Hickox, *Eng. Anal. Boundary Elements* **9**, 323 (1992).
9. P. A. Knipp and T. L. Reinecke, *Phys. Rev. B* **45**, 9091 (1992).
10. P. A. Knipp and T. L. Reinecke, *Phys. Rev. B* **45**, 10310 (1992).
11. P. A. Knipp and T. L. Reinecke, *Phys. Rev. B* **54**, 1880 (1996).
12. P. A. Knipp and T. L. Reinecke, *Solid State Electronics* **40**, 343 (1996).
13. P. A. Knipp and T. L. Reinecke, *Physica E* **2**, 920 (1998).
14. G. Arfken, *Mathematical Methods for Physicists*, 3rd ed. (Academic Press, Florida, 1985), p. 912.
15. These are LAPACK routines that may be downloaded from the Internet at the following URL, http://www.netlib.org/lapack.
16. G. S. Solomon, J. A. Trezza, A. F. Marshall, and J. S. Harris, *Phys. Rev. Lett.* **76**, 952 (1996).
17. Z. R. Wasilewski, S. Fafard, and J. P. McCaffrey, *J. Cryst. Growth* **201/202**, 1131 (1999).
18. L. F. Lester, A. Stintz, H. Li, T. C. Newell, E. A. Pease, B. A. Fuchs, and K. J. Malloy, *IEEE Photonics Tech. Lett.* **11**, 931 (1999).
19. G. T. Liu, A. Stintz, H. Li, K. J. Malloy, and L. F. Lester, *Electron. Lett.* **35**, 1163 (1999).
20. C. A. Brebbia, J. C. F. Telles, and L. C. Wrobel, *Boundary Element Techniques: Theory and Applications in Engineering* (Springer-Verlag, New York, 1984), p. 89.